An Integration Detection Approach for High-Speed Maneuvering Target in Airborne Coherent MIMO Radar

Mingxing Wang, Xiao Li, Xiaolong Li, Longji Gao, Desheng Chen, and Guolong Cui
School of Information and Communication Engineering
University of Electronic Science and Technology of China
Chengdu, China
Email: xiaolongliuestc@gmail.com

***Abstract*—This article addresses the multi-channel integration detection issue of high-speed maneuvering weak targets in airborne coherent multi-input multi-output (MIMO) radar. Coherent MIMO radar can significantly improve the detection performance through joint intra-channel and multi-channel fusion processing. Nevertheless, the range migration (RM) and Doppler frequency migration (DFM) are resulted from high-speed motion, and the envelope and phase differences among multi-channels are challenging. To address these limitations, we propose a multi-channel integration approach in generalized Radon-Fourier transform (GRFT) domain. First, the system and signal models are established. GRFT is utilized to accumulate intra-channel energy. Then, we construct a set of coupled equations, and estimate the target's position, speed and acceleration with the Newton-Raphson algorithm and solving linear equations. Based on the estimated outputs, the envelope alignment and phase compensation functions are constructed to eliminate the differences across channels. After that, the multi-channel fusion is realized in GRFT domain. The superiority of the proposed approach is shown via simulations.**

***Index Terms*—MIMO radar, high-speed maneuvering target, coherent integration**

I. Introduction

Coherent multi-input multi-output (MIMO) radar has received increasing attention because of its advantages in target parameter estimation and integration detection [1]–[4]. Compared to the monostatic radar, coherent MIMO radar can enhance the detection performance for high-speed maneuvering targets by signal-level fusion processing of multi-channel echoes [5]. However, target's high-speed motion induces range migration (RM) and Doppler frequency migration (DFM) in intra-channel echoes [6], [7]. In addition, due to the geometric differences of radar nodes relative to the target, the target's radial motion parameters over different nodes are different. Further, the envelope and phase differences across channels pose a challenge to multi-channel fusion. These issues seriously degrade the target detection performance.

This work was supported in part by the National Natural Science Foundation of China under Grant 62371113, in part by the Young Elite Scientists Sponsorship Program by CAST under Grant YESS20200082, in part by the Natural Science Foundation of Sichuan Province under Grant 2023NSFSC1386, and in part by the Aeronautical Science Foundation under Grant 2023Z017080001. (Corresponding author: Xiaolong Li.)

For intra-channel integration and fusion detection of the high-speed target, many excellent methods have been proposed in the past decade [7]–[11]. They could be divided into two kinds: non-coherent and coherent fusion approaches. The former usually sacrifices the accumulated performance at low signal-to-noise ratio (SNR) to obtain faster computational efficiency. However, for weak target detection, non-coherent accumulation may not be acceptable. The latter generally adopts the keystone transform (KT) [6], [7], [10] and Radon methods [8], [9], [12] to realize multi-pulse integration. In particular, generalized Radon-Fourier transform (GRFT) is an excellent algorithm with no obvious integration loss [9].

In addition to integrating intra-channel returns, another feasible strategy is to perform joint processing and fusion multi-channel echoes for MIMO radar [13]–[15]. The accumulation algorithm using signal reconstruction is proposed for stationary targets in [16]. The methods based on entropy and searching are presented for moving targets in [17] and [18], respectively. Nevertheless, the above algorithms do not consider the target's maneuverability. Therefore, it is crucial to address the multi-channel accumulation of high-speed maneuvering targets.

In this article, we propose a multi-channel fusion approach in GRFT domain. First, the geometric models of the high-speed maneuvering target and the MIMO radar are established. Then, GRFT is utilized to accumulate target energy of multi-pulse echoes. After that, we construct a set of coupled equations about the target kinetic parameters, and estimate the target's position, speed and acceleration by the Newton-Raphson algorithm and solving linear equations. Based on the estimated outputs, the envelope alignment and phase compensation functions are constructed to eliminate the differences across channels. Finally, the integration of multi-channel returns is realized in GRFT domain. Simulation results demonstrate the superiority of the proposed approach.

II. System and Signal Models

A. System Model

Considering that the airborne coherent MIMO radar includes M radar nodes in a 3-D Cartesian space, as shown in

Fig.1. In addition, we suppose that each radar node is a pulse Doppler radar system, and can transmit and receive signals simultaneously.

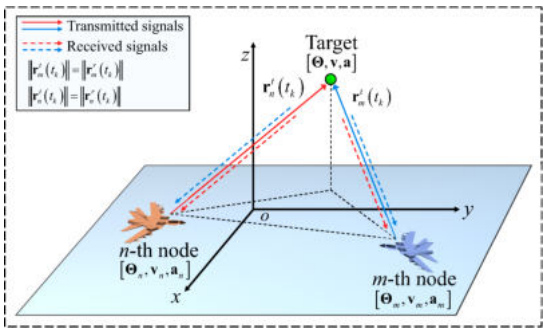

Fig. 1. The configuration of coherent MIMO radar.

The target's position, speed and acceleration are denoted as $\boldsymbol{\Theta} = [x_0, y_0, z_0]^{\mathrm{T}}$, $\boldsymbol{v} = [v_{x0}, v_{y0}, v_{z0}]^{\mathrm{T}}$ and $\boldsymbol{a} = [a_{x0}, a_{y0}, a_{z0}]^{\mathrm{T}}$, respectively. The $(\cdot)^{\mathrm{T}}$ represents the transpose operation. Moreover, let $\boldsymbol{\Theta}_m = [x_m, y_m, z_m]^{\mathrm{T}}$, $\boldsymbol{v}_m = [v_{xm}, v_{ym}, v_{zm}]^{\mathrm{T}}$ and $\boldsymbol{a}_m = [a_{xm}, a_{ym}, a_{zm}]^{\mathrm{T}}$, $m = 1, \cdots, M$ be the m-th radar node's position, speed and acceleration, respectively.

The instantaneous distance vector between the m-th transmitting node and the target could be given by

$$\boldsymbol{r}_m^t(t_k) = \boldsymbol{r}_m^t + (\boldsymbol{v}_m - \boldsymbol{v})\, t_k + \frac{1}{2}(\boldsymbol{a}_m - \boldsymbol{a})\, t_k^2, \tag{1}$$

where $\boldsymbol{r}_m^t = \boldsymbol{\Theta}_m - \boldsymbol{\Theta}$ represents the initial range vector from the m-th transmitting node to the target, $t_k, k = 1, 2, \cdots, K$ denotes the slow time with the pulse number K .

Similarly, the instantaneous range vector from the n-th receiving radar node for $n = 1, \cdots, M$ to the target is

$$\boldsymbol{r}_n^r(t_k) = \boldsymbol{r}_n^r + (\boldsymbol{v}_n - \boldsymbol{v})\, t_k + \frac{1}{2}(\boldsymbol{a}_n - \boldsymbol{a})\, t_k^2, \tag{2}$$

where $\boldsymbol{r}_n^r = \boldsymbol{\Theta}_n - \boldsymbol{\Theta}$ is the initial range vector between the n-th receiving node and the target.

Further, the equivalent distance of the (n, m) receive-transmit channel could be written as

$$r_{nm}(t_k) = \|\boldsymbol{r}_n^r(t_k)\| + \left\|\boldsymbol{r}_m^t(t_k)\right\|, \tag{3}$$

where $\|\cdot\|$ denotes the Euclidean norm.

Substituting (1) and (2) into (3), the Taylor expansion of $\|\boldsymbol{r}_m^t(t_k)\|$ and $\|\boldsymbol{r}_n^r(t_k)\|$ at $t_k = 0$ can be given by

$$\left\|\boldsymbol{r}_m^t(t_k)\right\| \approx r_m^t + v_m^t t_k + a_m^t t_k^2 + o\left(t_k^2\right), \tag{4a}$$
$$\|\boldsymbol{r}_n^r(t_k)\| \approx r_n^r + v_n^r t_k + a_n^r t_k^2 + o\left(t_k^2\right), \tag{4b}$$

where r_m^t and r_n^r represent respectively the initial transmitting and receiving ranges, which can be denoted as

$$r_m^t = \left\|\boldsymbol{r}_m^t\right\| = \|\boldsymbol{\Theta}_m - \boldsymbol{\Theta}\|, \tag{5a}$$
$$r_n^r = \|\boldsymbol{r}_n^r\| = \|\boldsymbol{\Theta}_n - \boldsymbol{\Theta}\|, \tag{5b}$$

v_m^t and v_n^r denote the relative transmitting and receiving speeds, respectively. We have

$$v_m^t = (\boldsymbol{\Theta}_m - \boldsymbol{\Theta}) \cdot (\boldsymbol{v}_m - \boldsymbol{v}) / \|\boldsymbol{\Theta}_m - \boldsymbol{\Theta}\|, \tag{6a}$$
$$v_n^r = (\boldsymbol{\Theta}_n - \boldsymbol{\Theta}) \cdot (\boldsymbol{v}_n - \boldsymbol{v}) / \|\boldsymbol{\Theta}_n - \boldsymbol{\Theta}\|, \tag{6b}$$

a_m^t and a_n^r are the relative transmitting and receiving accelerations, respectively. We can obtain

$$a_m^t = \left(\|\boldsymbol{v}_m - \boldsymbol{v}\|^2 + (\boldsymbol{\Theta}_m - \boldsymbol{\Theta}) \cdot (\boldsymbol{a}_m - \boldsymbol{a})\right) / \left(2\left\|\boldsymbol{r}_m^t\right\|\right) - \left((\boldsymbol{\Theta}_m - \boldsymbol{\Theta}) \cdot (\boldsymbol{v}_m - \boldsymbol{v})\right)^2 / \left(2\left\|\boldsymbol{r}_m^t\right\|^3\right), \tag{7a}$$

$$a_n^r = \left(\|\boldsymbol{v}_n - \boldsymbol{v}\|^2 + (\boldsymbol{\Theta}_n - \boldsymbol{\Theta}) \cdot (\boldsymbol{a}_n - \boldsymbol{a})\right) / \left(2\|\boldsymbol{r}_n^r\|\right) - \left((\boldsymbol{\Theta}_n - \boldsymbol{\Theta}) \cdot (\boldsymbol{v}_n - \boldsymbol{v})\right)^2 / \left(2\|\boldsymbol{r}_n^r\|^3\right), \tag{7b}$$

where $\boldsymbol{v} \cdot \boldsymbol{v}$ indicates the vector dot product. Substituting (4)-(7) into (3), the instant distance of the (n, m) receive-transmit channel could be rewritten as

$$r_{nm}(t_k) = r_m^t + r_n^r + \left(v_m^t + v_n^r\right) t_k + \left(a_m^t + a_n^r\right) t_k^2, \tag{8}$$

where $r_m^t + r_n^r$, $v_m^t + v_n^r$ and $a_m^t + a_n^r$ denote the equivalent initial distance, speed and acceleration, respectively.

B. Signal Model

The transmitting orthogonal signal is orthogonal frequency division multiplexing-linear frequency modulation signal. Specifically, the transmitting signal of the m-th node is

$$s_m(t) = p_m(t) \exp\left(j2\pi f_c t\right), \tag{9}$$

where f_c denotes the radar carrier frequency, $p_m(t)$ denotes the transmitting waveform of the m-th node, we have $p_m(t) = \sqrt{E}\,\mathrm{rect}\left(\frac{t}{T_p}\right) \exp\left(j2\pi\left((m-1)\Delta f t + 0.5\mu t^2\right)\right)$, where E is the transmitting energy, t represents the fast time, $\mathrm{rect}(\cdot)$ denotes the rectangular window function. Δf is the stepped-frequency, $\mu = B/T_p$ is the chirp rate with B indicating the bandwidth and T_p representing the pulse duration. Then, the echo of the (n, m) receive-transmit channel is formulated as

$$\tilde{y}_{nm}(t, t_k) = \beta_{nm} s_m\left(t - \frac{r_{nm}(t_k)}{c}\right), \tag{10}$$

where c is the light speed and β_{nm} denotes the propagation coefficient of the (n, m) receive-transmit channel [14], $\beta_{nm} = \sqrt{\frac{G_{n,r} G_{m,t} \lambda^2}{(4\pi)^3 (r_n^r)^2 (r_m^t)^2}}$, where $G_{n,r}$ and $G_{m,t}$ denote the antenna gain of the n-th and the m-th nodes, respectively. $\lambda = c/f_c$ is the signal wavelength.

Then, the receiving signal $\tilde{y}_n(t, t_k)$ of the the n-th radar node is $\tilde{y}_n(t, t_k) = \sum_{m=1}^{M} \tilde{y}_{nm}(t, t_k)$. It can be seen that $\tilde{y}_n(t, t_k)$ includes M radar node echoes. After performing down-conversion, the signal could be given by

$$\bar{y}_n(t, t_k) = \sum_{m=1}^{M} \beta_{nm} p_m\left(t - \frac{r_{nm}(t_k)}{c}\right) \exp\left(-j2\pi f_c \frac{r_{nm}(t_k)}{c}\right). \tag{11}$$

For MIMO radar, we need to construct matching filter to separate echo signals. The m-th matching filter is denoted as

$\omega_m(t) = p_m^*(-t), m = 1, 2, \cdots, M$, where the $(\cdot)^*$ represents the conjugate operation. Then, the result of the m-th matching filter at the n-th receiving radar node is

$$\begin{aligned} y_{nm}(t, t_k) &= \int_{-\infty}^{\infty} \bar{y}_n(\xi, t_k)\, \omega_m(t-\xi) d\xi \\ &= \beta_{nm} E \operatorname{sinc}\left(\pi B\left(t - \frac{r_{nm}(t_k)}{c}\right)\right) \exp\left(-j2\pi f_m \frac{r_{nm}(t_k)}{c}\right), \end{aligned} \tag{12}$$

where $\operatorname{sinc}(x) = \sin(x)/x$ and $f_m = f_c + (m-1)\Delta f$.

Let $r = ct/2$, and substituting (8) into (12), we can obtain

$$\begin{aligned} y_{nm}(r, t_k) = \beta_{nm} E \operatorname{sinc}&\left(\pi\left(\frac{r - (r_m^t + r_n^r)/2}{\rho_r}\right.\right. \\ &\left.\left. - \frac{\left(\left(v_m^t + v_n^r\right) t_k + \left(a_m^t + a_n^r\right) t_k^2\right)/2}{\rho_r}\right)\right) \\ &\times \exp\left(\frac{-j2\pi\left(\left(v_m^t + v_n^r\right) t_k + \left(a_m^t + a_n^r\right) t_k^2\right)}{\lambda}\right) \\ &\times \exp\left(\frac{-j2\pi f_m\left(r_m^t + r_n^r\right)}{c}\right), \end{aligned} \tag{13}$$

where $\rho_r = c/(2B)$ denotes distance resolution.

III. Coherent Integration Approach

In this section, GRFT is first utilized to accumulate the high-speed maneuvering target energy of the intra-channel returns. After that, a multi-channel fusion approach based on target parameter estimation is proposed in GRFT domain. The algorithm framework is presented in Fig.2.

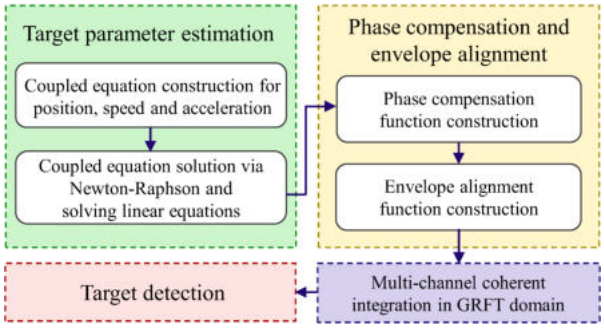

Fig. 2. Framework of the multi-channel fusion.

A. Intra-Channel Accumulation With GRFT

By matching the real motion trajectory of the target, the target's energy can be accurately integrated through GRFT. The GRFT searching parameters of range, speed and acceleration are written as $[-r_{\max}, r_{\max}]$, $[-v_{\max}, v_{\max}]$ and $[-a_{\max}, a_{\max}]$, respectively. The number of searching cells could be calculated by $\tilde{N}_r = \text{round}\left(2r_{\max}/\Delta_r\right), \tilde{N}_v = \text{round}\left(2v_{\max}/\Delta_v\right)$, and $\tilde{N}_a = \text{round}\left(2a_{\max}/\Delta_a\right)$, respectively. The round$(\cdot)$ indicates the rounding to the nearest integer. The Δ_r, Δ_v and Δ_a are the searching intervals of range, speed and acceleration, respectively.

As a result, the discrete indexes of the range, speed and acceleration are given by

$$r_s(\varepsilon) = -r_{\max} + \varepsilon\Delta_r, \varepsilon = 1, 2, \cdots, \tilde{N}_r, \tag{14a}$$

$$v_s(\gamma) = -v_{\max} + \gamma\Delta_v, \gamma = 1, 2, \cdots, \tilde{N}_v, \tag{14b}$$

$$a_s(\chi) = -a_{\max} + \chi\Delta_a, \chi = 1, 2, \cdots, \tilde{N}_a. \tag{14c}$$

The intra-channel accumulation of $y_{nm}(r, t_q)$ by GRFT is expressed as (15). When searching parameters match target's equivalent kinetic parameters. (15) could be rewritten as

$$\begin{aligned} &G_{nm}\left(r_s(\varepsilon_{nm}),\ v_s(\gamma_{nm}), a_s(\chi_{nm})\right) \\ &\quad \approx \beta_{nm} KE \operatorname{sinc}\left(\pi\left(r_s(\varepsilon_{nm}) - r_m^t - r_n^r\right)\right) \\ &\qquad \times \delta\left(v_s(\gamma_{nm}) - v_m^t - v_n^r\right) \\ &\qquad \times \delta\left(a_s(\chi_{nm}) - a_m^t - a_n^r\right) \\ &\qquad \times \exp\left(\frac{-j2\pi f_m(r_m^t + r_n^r)}{c}\right), \end{aligned} \tag{16}$$

where $\delta(\cdot)$ denotes the Dirichlet function, $r_s(\varepsilon_{nm}) = r_m^t + r_n^r$, $v_s(\gamma_{nm}) = v_m^t + v_n^r$ and $a_s(\chi_{nm}) = a_m^t + a_n^r$. Therefore, the integrated peak position of target is located at $(\varepsilon_{nm}, \gamma_{nm}, \chi_{nm})$ in the GRFT domain for the (n, m) receive-transmit channel.

B. Target Parameter Estimation

In this subsection, the detailed procedure of the target parameter estimation is provided, including the coupling equation construction and solution.

1) Coupling equation construction: We utilize the relationship between target's peak positions in GRFT domain and the real target motion parameters to establish the coupled equations. For the (m, m), (n, n) and (i, i) receive-transmit channels, the focused peak points in GRFT domain are $(r_s(\varepsilon_{mm}), v_s(\gamma_{mm}), a_s(\chi_{mm}))$, $(r_s(\varepsilon_{nn}), v_s(\gamma_{nn}), a_s(\chi_{nn}))$, $(r_s(\varepsilon_{ii}), v_s(\gamma_{ii}), a_s(\chi_{ii}))$, respectively. Then, for convenience, we denote $\boldsymbol{r}_s = [r_s(\varepsilon_{mm}), r_s(\varepsilon_{nn}), r_s(\varepsilon_{ii})]^{\mathrm{T}} \in \mathbb{R}^{3\times 1}$, $\boldsymbol{v}_s = [v_s(\gamma_{mm}), v_s(\gamma_{nn}), v_s(\gamma_{ii})]^{\mathrm{T}} \in \mathbb{R}^{3\times 1}$ and $\boldsymbol{a}_s = [a_s(\chi_{mm}), a_s(\chi_{nn}), a_s(\chi_{ii})]^{\mathrm{T}} \in \mathbb{R}^{3\times 1}$.

$$\begin{aligned} G_{nm}(r_s(\varepsilon), v_s(\gamma), a_s(\chi)) = \sum_{k=1}^{K} \beta_{nm} E \operatorname{sinc}&\left(\pi\left(\frac{\left(r_s(\varepsilon) - r_m^t - r_n^r\right) + \left(v_s(\gamma) - v_m^t - v_n^r\right) t_k + \left(a_s(\chi) - a_m^t - a_n^r\right) t_k^2}{\rho_r}\right)\right) \\ &\times \exp\left(\frac{-j2\pi f_m(r_m^t + r_n^r)}{c}\right) \exp\left(\frac{j2\pi\left(v_s(\gamma) - v_m^t - v_n^r\right) t_k}{\lambda}\right) \exp\left(\frac{j2\pi\left(a_s(\chi) - a_m^t - a_n^r\right) t_k^2}{\lambda}\right) \\ &\varepsilon = 1, 2, \cdots, \tilde{N}_r; \gamma = 1, 2, \cdots, \tilde{N}_v; \chi = 1, 2, \cdots, \tilde{N}_a. \end{aligned} \tag{15}$$

$$\mathbf{a}_s\left(\chi_{mm}\right)=\left(\begin{array}{c}\left(v_{xm}-v_{x0}\right)^2+\left(x_m-x_0\right)\left(a_{xm}-\hat{a}_{x0}\right)\\+\left(v_{ym}-v_{y0}\right)^2+\left(y_m-y_0\right)\left(a_{ym}-\hat{a}_{y0}\right)\\+\left(v_{zm}-v_{z0}\right)^2+\left(z_m-z_0\right)\left(a_{zm}-\hat{a}_{z0}\right)\end{array}\right)/\left(2r_s\left(\varepsilon_{mm}\right)\right)-\left(\begin{array}{c}\left(x_m-x_0\right)\left(v_{xm}-v_{x0}\right)\\+\left(y_m-y_0\right)\left(v_{ym}-v_{y0}\right)\\+\left(z_m-z_0\right)\left(v_{zm}-v_{z0}\right)\end{array}\right)^2/\left(2\left(r_s\left(\varepsilon_{mm}\right)\right)^3\right). \tag{21}$$

$$\boldsymbol{b}_a(1)=\left[\begin{array}{c}\left(\left(x_m-x_0\right)\left(v_{xm}-v_{x0}\right)+\left(y_m-y_0\right)\left(v_{ym}-y_{x0}\right)+\left(z_m-z_0\right)\left(v_{zm}-v_{z0}\right)\right)^2/\left(r_s\left(\varepsilon_{mm}\right)\right)^2+2a_s\left(\chi_{mm}\right)r_s\left(\varepsilon_{mm}\right)\\-\left(v_{xm}-v_{x0}\right)^2-\left(x_m-x_0\right)a_{xm}-\left(v_{ym}-v_{y0}\right)^2-\left(y_m-y_0\right)a_{ym}-\left(v_{zm}-v_{z0}\right)^2-\left(z_m-z_0\right)a_{zm},\end{array}\right]. \tag{23}$$

According to (5), the expression for the peak locations of GRFT outputs and the target positions can be expressed as

$$\left\{\begin{array}{l}2\left\|\boldsymbol{\Theta}_m-\hat{\boldsymbol{\Theta}}\right\|=r_s\left(\varepsilon_{mm}\right)\\2\left\|\boldsymbol{\Theta}_n-\hat{\boldsymbol{\Theta}}\right\|=r_s\left(\varepsilon_{nn}\right)\\2\left\|\boldsymbol{\Theta}_i-\hat{\boldsymbol{\Theta}}\right\|=r_s\left(\varepsilon_{ii}\right),\end{array}\right. \tag{17}$$

where $\hat{\boldsymbol{\Theta}}=[\hat{x}_0,\hat{y}_0,\hat{z}_0]^{\mathrm{T}}\in\mathbb{R}^{3\times1}$ is the estimated target position.

In addition, as shown in (6), we can also achieve the relationship between the speed of GRFT results, and the kinetic parameters of the target and radar nodes, i.e.,

$$\left\{\begin{array}{l}v_s\left(\gamma_{mm}\right)=\frac{1}{r_s\left(\varepsilon_{mm}\right)}\left(\begin{array}{c}\left(x_m-x_0\right)\left(v_{xm}-\hat{v}_{x0}\right)\\+\left(y_m-y_0\right)\left(v_{ym}-\hat{v}_{y0}\right)\\+\left(z_m-z_0\right)\left(v_{zm}-\hat{v}_{z0}\right)\end{array}\right)\\v_s\left(\gamma_{nn}\right)=\frac{1}{r_s\left(\varepsilon_{nn}\right)}\left(\begin{array}{c}\left(x_n-x_0\right)\left(v_{xn}-\hat{v}_{x0}\right)\\+\left(y_n-y_0\right)\left(v_{yn}-\hat{v}_{y0}\right)\\+\left(z_n-z_0\right)\left(v_{zn}-\hat{v}_{z0}\right)\end{array}\right)\\v_s\left(\gamma_{ii}\right)=\frac{1}{r_s\left(\varepsilon_{ii}\right)}\left(\begin{array}{c}\left(x_i-x_0\right)\left(v_{xi}-\hat{v}_{x0}\right)\\+\left(y_i-y_0\right)\left(v_{yi}-\hat{v}_{y0}\right)\\+\left(z_i-z_0\right)\left(v_{zi}-\hat{v}_{z0}\right)\end{array}\right).\end{array}\right. \tag{18}$$

Further, the matrix form of (18) could be given by

$$\boldsymbol{C}_v\hat{\boldsymbol{v}}-\boldsymbol{b}_v=\mathbf{0}, \tag{19}$$

where $\boldsymbol{C}_v=\left[\boldsymbol{c}_x^v,\boldsymbol{c}_y^v,\boldsymbol{c}_z^v\right]\in\mathbb{R}^{3\times3}$ is defined as (20), $\hat{\boldsymbol{v}}=[\hat{v}_x,\hat{v}_y,\hat{v}_z]^{\mathrm{T}}\in\mathbb{R}^{3\times1}$ indicates the estimated target speed, $\boldsymbol{b}_v\in\mathbb{R}^{3\times1}$ denotes the coefficients, and $\boldsymbol{b}_v(1)=[v_s\left(\gamma_{mm}\right)r_s\left(\varepsilon_{mm}\right)-\left(x_m-x_0\right)v_{xm}-\left(y_m-y_0\right)v_{ym}-\left(z_m-z_0\right)v_{zm}]$, where $\boldsymbol{b}_v(1)$ represents the 1-st element of $\boldsymbol{b}_v$. Similarly, for radar nodes n and i, we can achieve $\boldsymbol{b}_v(2)$ and $\boldsymbol{b}_v(3)$, respectively. $\mathbf{0}\in\mathbb{R}^{3\times1}$ is a zero column vector.

$$\left\{\begin{array}{ll}\boldsymbol{c}_x^v&=\left[\begin{array}{cccc}x_0-x_m&x_0-x_n&x_0-x_i\end{array}\right]^{\mathrm{T}}\in\mathbb{R}^{3\times1}\\\boldsymbol{c}_y^v&=\left[\begin{array}{cccc}y_0-y_m&y_0-y_n&y_0-y_i\end{array}\right]^{\mathrm{T}}\in\mathbb{R}^{3\times1}\\\boldsymbol{c}_z^v&=\left[\begin{array}{cccc}z_0-z_m&z_0-z_n&z_0-z_i\end{array}\right]^{\mathrm{T}}\in\mathbb{R}^{3\times1}.\end{array}\right. \tag{20}$$

As described in (7), the acceleration equation between the GRFT outputs and the target and radar motion parameters could be expressed as (21) for the node m. Then the similar expression for nodes n and i can also be obtained. The matrix expression could be expressed as

$$\boldsymbol{C}_a\hat{\boldsymbol{a}}-\boldsymbol{b}_a=\mathbf{0}, \tag{22}$$

where $\hat{\boldsymbol{a}}=[\hat{a}_x,\hat{a}_y,\hat{a}_z]^{\mathrm{T}}\in\mathbb{R}^{3\times1}$ is the estimated target's acceleration vector, $\boldsymbol{b}_a\in\mathbb{R}^{3\times1}$ is the acceleration equation coefficients and the $\boldsymbol{b}_a(1)$ is denoted (23). Substituting n and i, we can get $\boldsymbol{b}_a(2)$ and $\boldsymbol{b}_a(3)$, respectively. $\boldsymbol{C}_a=\left[\boldsymbol{c}_x^a,\boldsymbol{c}_y^a,\boldsymbol{c}_z^a\right]\in\mathbb{R}^{3\times3}$ and are denoted as

$$\left\{\begin{array}{ll}\boldsymbol{c}_x^a&=\left[\begin{array}{cccc}x_0-x_m&x_0-x_n&x_0-x_i\end{array}\right]^{\mathrm{T}}\in\mathbb{R}^{3\times1}\\\boldsymbol{c}_y^a&=\left[\begin{array}{cccc}y_0-y_m&y_0-y_n&y_0-y_i\end{array}\right]^{\mathrm{T}}\in\mathbb{R}^{3\times1}\\\boldsymbol{c}_z^a&=\left[\begin{array}{cccc}z_0-z_m&z_0-z_n&z_0-z_i\end{array}\right]^{\mathrm{T}}\in\mathbb{R}^{3\times1}.\end{array}\right. \tag{24}$$

So far, we obtain coupled equations over the target location, speed and acceleration, as described in (17), (19) and (22).

2) Coupling equation solution: The algorithm for solving the coupling equations is presented in this subsection.

Position Estimation: For the estimated position, the (17) can be rewritten as

$$\left\{\begin{array}{l}\varrho\left(\boldsymbol{\Theta}_m,\hat{\boldsymbol{\Theta}},r_s\left(\varepsilon_{mm}\right)\right)=2\left\|\boldsymbol{\Theta}_m-\hat{\boldsymbol{\Theta}}\right\|-r_s\left(\varepsilon_{mm}\right)\\\varrho\left(\boldsymbol{\Theta}_n,\hat{\boldsymbol{\Theta}},r_s\left(\varepsilon_{nn}\right)\right)=2\left\|\boldsymbol{\Theta}_n-\hat{\boldsymbol{\Theta}}\right\|-r_s\left(\varepsilon_{nn}\right)\\\varrho\left(\boldsymbol{\Theta}_i,\hat{\boldsymbol{\Theta}},r_s\left(\varepsilon_{ii}\right)\right)=2\left\|\boldsymbol{\Theta}_i-\hat{\boldsymbol{\Theta}}\right\|-r_s\left(\varepsilon_{ii}\right).\end{array}\right. \tag{25}$$

(25) is a set of nonlinear equations with respect to $\hat{\boldsymbol{\Theta}}$. We solve it by means of Newton-Raphson algorithm [19]. Finally, we can achieve the estimated target position $\hat{\boldsymbol{\Theta}}=[\hat{x}_0,\hat{y}_0,\hat{z}_0]^{\mathrm{T}}$.

Velocity Estimation: Substituting $\hat{\boldsymbol{\Theta}}$ into $\boldsymbol{C}_v$ and $\boldsymbol{b}_v$, the $\hat{\boldsymbol{C}}_v$ and $\hat{\boldsymbol{b}}_v$ could be estimated. Then, (19) can be recast as

$$\hat{\boldsymbol{C}}_v\hat{\boldsymbol{v}}-\hat{\boldsymbol{b}}_v=\mathbf{0}. \tag{26}$$

Considering that radar nodes are independent of each other. Consequently, we can obtain $\det(\hat{\boldsymbol{C}}_v)\neq0$, where $\det(\cdot)$ denotes the matrix determinant. After that, the $\hat{\boldsymbol{v}}=[\hat{v}_{x0},\hat{v}_{y0},\hat{v}_{z0}]^{\mathrm{T}}$ could be expressed as $\hat{\boldsymbol{v}}=\left(\hat{\boldsymbol{C}}_v\right)^{-1}\hat{\mathbf{b}}_v$.

Acceleration Estimation: We substitute $\hat{\boldsymbol{\Theta}}$ and $\hat{\boldsymbol{v}}$ into (22) and have

$$\hat{\boldsymbol{C}}_a\hat{\boldsymbol{a}}-\hat{\boldsymbol{b}}_a=\mathbf{0}. \tag{27}$$

Then, the acceleration $\hat{\boldsymbol{a}}=[\hat{a}_{x0},\hat{a}_{y0},\hat{a}_{z0}]^{\mathrm{T}}$ could be estimated by (27), i.e. $\hat{\boldsymbol{a}}=\left(\hat{\boldsymbol{C}}_a\right)^{-1}\hat{\mathbf{b}}_a$.

C. Phase Compensation and Envelope Alignment

To achieve the integration result of multi-channel returns, we construct the inter-channel envelope alignment and phase compensation functions using the estimated target parameters.

More specifically, the (n,m) receive-transmit channel is used as the reference channel. By utilizing the estimated position, speed and acceleration of the target and equations (5)-(7), we can get the estimated $\hat{r}_s(\varepsilon_{mi})$, $\hat{v}_s(\gamma_{mi})$ and $\hat{a}_s(\chi_{mi})$. Correspondingly, the phase compensation function of the (m,i) receive-transmit channel is given by

$$H_{mi}^{p}(\boldsymbol{r}_s) = \exp\left(\frac{j2\pi(-f_n \boldsymbol{r}_s(2) + f_i \hat{r}_s(\varepsilon_{mi})}{c}\right), \tag{28}$$

where $\boldsymbol{r}_s(2)$ represents the 2-nd element of $\boldsymbol{r}_s$.

The location alignment function is expressed as

$$\begin{aligned} H_{mi}^{e}(\boldsymbol{r}_s, \boldsymbol{v}_s, \boldsymbol{a}_s, r_s(\varepsilon), v_s(\gamma), a_s(\chi)) = \\ \delta\left(r_s(\varepsilon) - (\boldsymbol{r}_s(2) - \hat{r}_s\left(\varepsilon_{mi}\right))\right) \\ \times \delta\left(v_s(\gamma) - (\boldsymbol{v}_s(2) - \hat{v}_s(\gamma_{mi}))\right) \\ \times \delta\left(a_s(\chi) - (\boldsymbol{a}_s(2) - \hat{a}_s\left(\chi_{mi}\right))\right), \end{aligned} \tag{29}$$

where $\boldsymbol{v}_s(2)$ and $\boldsymbol{a}_s(2)$ are the 2-nd elements of $\boldsymbol{v}_s$ and $\boldsymbol{a}_s$, respectively.

Using (28) and (29), the inter-channel accumulation is

$$\begin{aligned} &\Upsilon(\boldsymbol{r}_s, \boldsymbol{v}_s, \boldsymbol{a}_s, r_s(\varepsilon), v_s(\gamma), a_s(\chi)) \\ &= \sum_{m=1}^{M}\sum_{i=1}^{M} G_{mi} H_{mi}^{p} H_{mi}^{e} \\ &= \sum_{m=1}^{M}\sum_{i=1}^{M} \beta_{mi} K E \operatorname{sinc}\left(\pi\left(r_s(\varepsilon) - r_n^t - r_m^r\right)\right) \\ &\quad \times \delta\left(v_s(\gamma) - v_n^t - v_m^r\right) \delta\left(a_s(\chi) - a_n^t - a_m^r\right) \\ &\quad \times \exp\left(\frac{-j2\pi f_m\left(r_n^t + r_m^r\right)}{c}\right). \end{aligned} \tag{30}$$

As illustrated in (30), the energy of target among multiple channels is effectively accumulated. Finally, the target detection is carried out based on the focused result [14].

IV. Numerical Results

In this section, the different simulation scenarios are illustrated to evaluate the algorithm performance. Besides, the GRFT [9], the generalized second-order keystone transform-modified product cubic phase function (GSKT-MPCPF) [6] and the modified Radon-Fourier transform (MRFT) [12] are provided for comparison.

We first give the radar parameters, as presented in Table I. Consider three radar nodes, the positions are $(1187, 1980.3, 10100)$ m, $(1200, 2000.2, 9928)$ m and $(1400, 2020.2, 9928)$ m, respectively. The speeds are $(672, 659.4, 669)$ m/s, $(719, 638.9, 589.9)$ m/s and $(719, 631.4, 588)$ m/s, respectively. The accelerations are $(10, 35.92, 25)$ m/s^2, $(11, 73.36, 15)$ m/s^2 and $(12, 114.25, 12)$ m/s^2 , respectively. In addition, the target's location, speed and acceleration are $(1300, 40000, 10000)$ m, $(-705, -590, -655)$ m/s and $(-78, 60, -67)$ m/s^2.

TABLE I
Radar Parameters.

Parameter	Symbol	Value
Carrier frequency	f_c	0.2 GHz
Bandwidth	B	1 MHz
Pulse repetition time	T_s	2 ms
Pulse duration	T_r	100 us
Sampling frequency	f_s	30 MHz
Pulse number	Q	128
Step-frequency	Δf	1 MHz

A. Integration Performance Comparison

This subsection presents the integration ability for different methods in high and low SNR scenarios. Under high SNR environment, Fig.3(a) illustrates the range compression result of the $(1,1)$ receive-transmit channel, where the SNR after range compression is 8 dB. The range-velocity and velocity-acceleration slices are given via the GRFT in Figs.3(b) and (c). In addition, the integration outputs of the GSKT-MPCPF, MRFT and the proposed method are shown in Figs.3(d), (e) and (f). It could be observed that the proposed approach obtains the best accumulation performance.

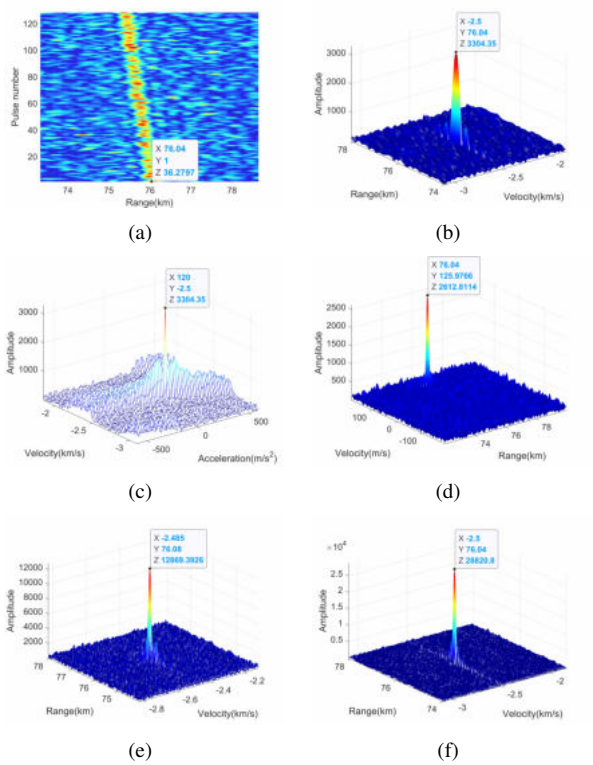

(a) (b) (c) (d) (e) (f)

Fig. 3. The high SNR scenario. (a) Range compression reult. (b) The range-velocity slice of the GRFT. (c) The velocity-acceleration slice of the GRFT. (d) GSKT-MPCPF. (e) MRFT. (f) The proposed approach.

Simulation experiments are addressed under low SNR scenarios. The SNR after range compression is set as -18 dB. Figs.4(a), (b) and (c) show the range-velocity slice with the

GRFT, the integration output of the GSKT-MPCPF and the accumulation result of the MRFT, respectively. Note that the above three methods cannot provide effective integration results. As a comparison, the target's energy is accumulated to a distinct peak using the proposed approach, as shown in Fig.4(d).

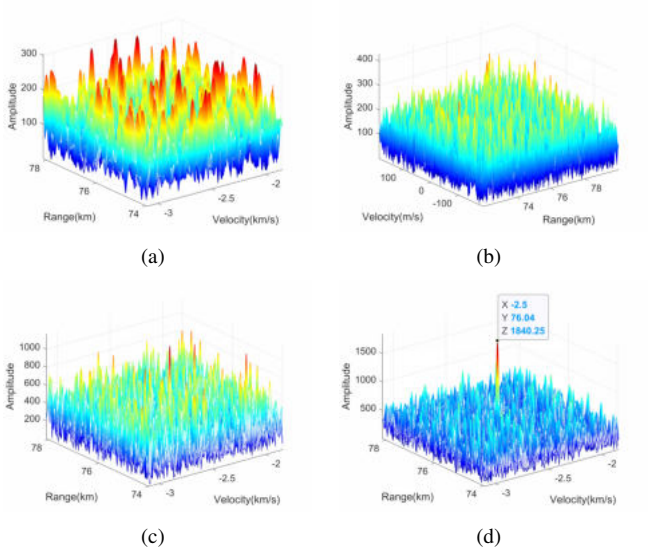

Fig. 4. The low SNR scenario. (a) The range-velocity slice of the GRFT. (b) GSKT-MPCPF. (c) MRFT. (d) The proposed approach.

B. Detection Performance Comparison

This subsection compares the detection probability for different methods. The simulation parameters are the same as in Section IV-A, and the false alarm rate is 10^{-4}. The detection curves are plotted through 500 Monte Carlo under each SNR. As illustrated in Fig.5, it can be noticed that the proposed approach performs the best detection performance compared to the GSKT-MPCPF, GRFT and MRFT. This is an expected result because the proposed algorithm accurately accumulates multi-channel target energy. Moreover, Fig.6 gives the detection curves via the proposed approach for different number of radar nodes. Notice that as the number of radar nodes increases, coherent MIMO radar system can obtain superior detection performance using the proposed method.

V. Conclusion

In this article, a multi-channel coherent fusion approach in GRFT domain was proposed in airborne coherent MIMO radar systems. The proposed method considered the integration detection of high-speed maneuvering weak targets in 3-D space. Unlike the traditional coherent accumulation algorithm which only accumulated multi-pulse echo energy, the proposed approach made full use of the advantages of MIMO radar multi-channel returns, and showed significant performance improvements in integration ability and detection probability. Numerical results illustrated the superiority of the proposed approach.

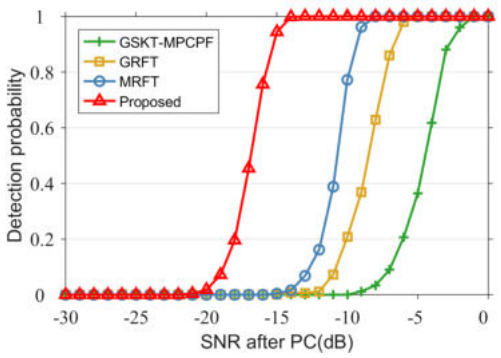

Fig. 5. Detection probability curves of different algorithms.

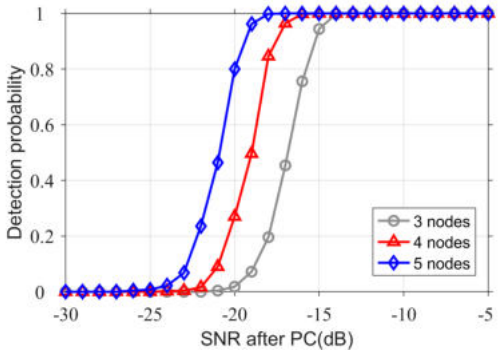

Fig. 6. Detection probability curves of varying radar node numbers.

References

[1] F. C. Robey, S. Coutts, D. Weikle, J. C. McHarg, and K. Cuomo, "MIMO radar theory and experimental results," in *Proc. Conf. Rec. 38th Asilomar Conf. Signals, Syst. Comput.*, Pacific Grove, CA, USA, vol. 1, 2004, pp. 300-304.

[2] S. Yang, H. Tan, W. Yi, and L. Kong, "Discrete grid based detection strategies for distributed MIMO radars," in *Proc. 22th Int. Conf. Inf. Fusion (FUSION)*, Ottawa, ON, Canada, 2019, pp. 1-7.

[3] E. Fishler, A. Haimovich, R. S. Blum, L. J. Cimini, D. Chizhik, and R. A. Valenzuela, "Spatial diversity in radars-models and detection performance," *IEEE Trans. Signal Process.*, vol. 54, no. 3, pp. 823-838, 2006.

[4] J. Li and P. Stoica, "MIMO radar with colocated antennas," *IEEE Signal Process. Mag.*, vol. 24, no. 5, pp. 106-114, 2007.

[5] Y. Yang and R. S. Blum, "Phase synchronization for coherent MIMO radar: algorithms and their analysis," *IEEE Trans. Signal Process.*, vol. 59, no. 11, pp. 5538-5557, 2011.

[6] J. Zhang, T. Ding, and L. Zhang, "Longtime coherent integration algorithm for high-speed maneuvering target detection using space-based bistatic radar," *IEEE Trans. Geosci. Remote Sens.*, vol. 60, pp. 1-16, 2022, Art no. 5100216.

[7] P. Huang, G. Liao, Z. Yang, X.-G. Xia, J.-T. Ma, and J. Ma, "Long-time coherent integration for weak maneuvering target detection and high-order motion parameter estimation based on keystone transform," *IEEE Trans. Signal Process.*, vol. 64, no. 15, pp. 4013-4026, 2016.

[8] X. Chen, J. Guan, N. Liu, and Y. He, "Maneuvering target detection via Radon-fractional Fourier transform-based long-time coherent integration," *IEEE Trans. Signal Process.*, vol. 62, no. 4, pp. 939-953, 2014.

[9] J. Xu, J. Yu, Y. Peng, and X.-G. Xia, "Radon-Fourier transform (RFT) for radar target detection (I): generalized Doppler filter bank processing," *IEEE Trans. Aerosp. Electron. Syst.*, vol. 47, no. 2, pp. 1186-1202, 2011.

[10] J. Tian, W. Cui, X.-G. Xia, and S.-L. Wu, "Parameter estimation of ground moving targets based on SKT-DLVT processing," *IEEE Trans. Comput. Imaging*, vol. 2, no. 1, pp. 13-26, 2016.

[11] J. Zheng, T. Su, H. Liu, G. Liao, Z. Liu, and Q. H. Liu, "Radar high-speed target detection based on the frequency-domain deramp-keystone transform," *IEEE J. Sel. Topics Appl. Earth Observ. Remote Sens.*, vol. 9, no. 1, pp. 285-2 94, 2016.

[12] X. Li, Y. Yang, Z. Sun, G. Cui, and T. S. Yeo, "Multi-Frame integration method for radar detection of weak moving target," *IEEE Trans. Veh. Technol.*, vol. 70, no. 4, pp. 3609-3624, 2021.

[13] A. De Maio, S. Han, and D. Orlando, "Adaptive radar detectors based on the observed FIM," *IEEE Trans. Signal Process.*, vol. 66, no. 14, pp. 3838-3847, 2018.

[14] H. Li, F. Wang, C. Zeng, and M. A. Govoni, "Signal detection in distributed MIMO radar with non-orthogonal waveforms and sync errors," *IEEE Trans. Signal Process.*, vol. 69, pp. 3671-3684, 2021.

[15] M. Wang, X. Li, L. Gao, Z. Sun, G. Cui, and T. S. Yeo, "Signal accumulation method for high-speed maneuvering target detection using airborne coherent MIMO radar," *IEEE Trans. Signal Process.*, vol. 71, pp. 2336-2351, 2023.

[16] X. Liu, Z. Xu, X. Liu, S. Chen, and S. Xiao, "A clean signal reconstruction approach for coherently combining multiple radars," *EURASIP J. Adv. in Signal Process.*, vol. 2018, no. 1, pp. 1-11, 2018.

[17] M. Wang, X. Li, T. Fan, Z. Sun, C. Wang, and G. Cui, "Entropy-Based coherent integration method for moving target detection using phased-MIMO radar," in *Proc. IEEE Radar Conf.*, Atlanta, GA, USA, 2021, pp. 1-6.

[18] M. Wang, X. Li, Z. Zhang, G. Cui, and T. S. Yeo, "Coherent integration and parameter estimation for high-speed target detection with bistatic MIMO radar," *IEEE Trans. Geosci. Remote Sens.*, vol. 61, pp. 1-15, 2023, Art no. 5107915.

[19] S. Boyd and L. Vandenberghe, *Convex Optimization*. Cambridge, U.K.: Cambridge Univ. Press., 2004.